Influences of Energy Density on Porosity and Microstructure of Selective Laser Melted 17-4PH Stainless Steel

Hengfeng Gu*, Haijun Gong*, Deepankar Pal*, Khalid Rafi*, Thomas Starr†, Brent Stucker*

*Department of Industrial Engineering, †Department of Chemical Engineering,
J. B. Speed School of Engineering, University of Louisville, Louisville, KY 40292

Abstract

Energy density, which directly impacts the properties of as-built parts, is a key factor in the metal selective laser melting (SLM) process. This paper studies the influences of energy density on porosity and microstructure of SLM 17-4PH stainless steel parts. Experiments were carried out by varying processing parameters to change energy density. Porosity was estimated using the Archimedes method and image analysis. Microstructures were investigated through optical and electron microscopy. The experimental results were discussed regarding porosity formation and microstructure characterization.

Introduction

Laser energy density is considered a key factor that affects the properties of as-built parts fabricated by SLM processing. The widely used volume based energy density E (J/mm^3) is defined in equation (1), where P is laser power (W), v is scan speed (mm/s), h is hatch spacing (mm) and t is layer thickness (mm) [1].

$$E = \frac{P}{v * h * t} \tag{1}$$

Although energy density is a crucial indicator of energy input, there are few publications [1, 2] discussing the relationship between energy density and some fundamental properties of as-built parts such as porosity, microstructure and phase proportion in a comprehensive manner.

17-4PH stainless steel is a commonly used alloy in a wide range of areas including commercial, defense and medical sectors [3]. Martensite and metastable austenite are typical phases observed in parts fabricated by SLM processing [4].Previous studies with 17-4PH stainless steels using SLM were mainly focused on the influences of post heat-treatment on mechanical properties of the part [3,5]. Few studies have been done which concentrate on changes of the as-built part properties under various processing parameters using 17-4PH stainless steel powders in SLM [2].

Better understanding is required on the influences of energy density on as-built porosity, microstructures and phase proportion while using 17-4PH stainless steel powders in SLM in order to develop optimal processing parameters. These parameters will lead to fabrication of better quality parts manufactured using specific 17-4PH stainless steel powders.

Materials and experiment procedures

Materials

Stainless steel powders used for coupon manufacturing were acquired from EOS with product specification GP1 17-4PH (EOS GmbH, Munich, Germany). This type of powder is gas atomized in a nitrogen environment. The chemical composition of GP1 powder is shown in table 1 [6]. The mean volume diameter is 37.13μm with a standard deviation of 9.85μm. Figure 1 shows the typical morphology of GP1 powders using a scanning electron microscope (FEI Nova Nano SEM). The majority of these powders exhibit spherical shapes, while some tiny powders are attached to bigger powders. GP1 powders appear to be a good fit for the SLM process.

Table 1 Chemical composition of GP1 powder

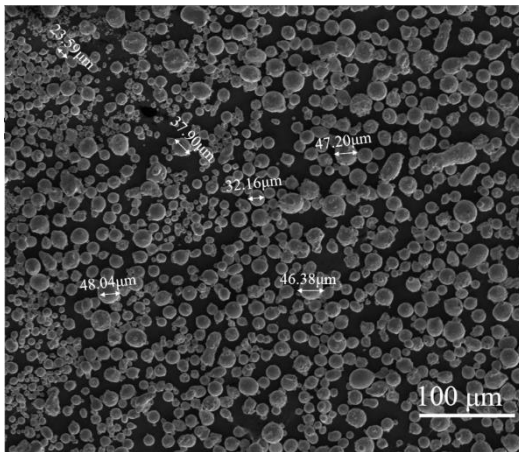| Elements	Cr	Ni	Cu	Mn	Si	Mo	Nb	C
Composition (wt%)	15-17.5	3-5	3-5	max. 1	max. 1	max. 0.5	0.15-0.45	max. 0.07

Figure 1 EOS GP1 powder SEM image

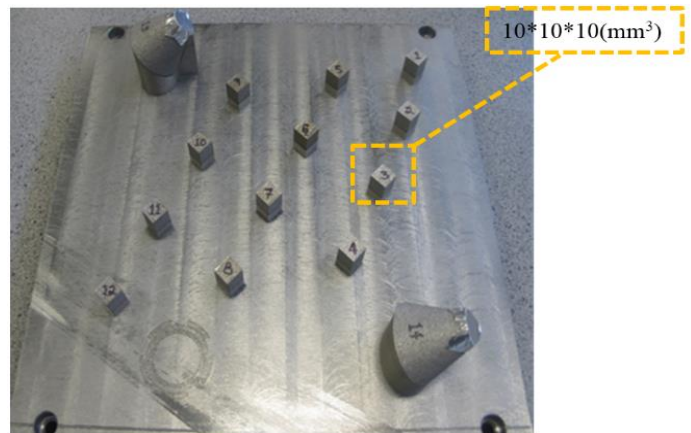Figure 2 As-built test coupons on the build plate

Test coupon manufacturing process

Twelve test coupons with cubical dimensions of 10*10*10mm, shown in figure 2, were manufactured using an EOS M270 Direct Metal Laser Sintering (DMLS) machine in a nitrogen purging atmosphere. Two types of processing parameter sets were defined by varying laser power and scan speed, as shown in table 2. The left column of table 2 describes the parameter set under various energy densities by solely changing the scan speed while keeping the laser power at a constant level. The right column shows a set of parameter combinations which include the EOS recommended parameters and other parameters which result in the same optimal energy density by changing laser power and scan speed simultaneously. A 100μm hatch spacing and a 40μm layer thickness were applied to all processing conditions.

Table 2 Processing parameters for coupon manufacturing

	Energy density varies				Energy density constant		
No.	Laser Power (W)	Scan Speed (mm/s)	ED(J/mm^3)	No.	Laser Power (W)	Scan Speed (mm/s)	ED (J/mm^3)
1	195	1200	41	a/5*	195	800	61
2	195	1100	44	b	170	697	61
3	195	1000	49	c	145	594	61
4	195	900	54	d	120	492	61
5/a*	195	800	61	e	95	389	61
6	195	700	70	f	70	287	61
7	195	600	81				

* Manufacturer's recommended parameters

Porosity measurements and characterization techniques

Two porosity measurement techniques were employed on the stainless steel coupons after the support separation from the build plate using a high speed band saw.

Archimedes method was applied to measure the density for each coupon at first (ASTM B962-13). Masses of each coupon in air and water were measured independently 3 times using an electronic balance with ±1mg accuracy. Similarly, average masses were calculated by taking the mean mass in air and water for each coupon and denoted using m_a and m_{fl} respectively. Average masses were inserted into equation (2) below to obtain coupon density ρ_p, where ρ_{fl} is the density of water [7].

$$\rho_p = \frac{m_a}{m_a - m_{fl}} \times \rho_{fl} \qquad (2)$$

Equation (3) was used to convert measured test coupon density ρ_p to its corresponding porosity $\emptyset$, where ρ_{tv} is the threshold density value for a fully dense part.

$$\emptyset = \frac{\rho_p}{\rho_{tv}} \qquad (3)$$

Based on results from analysis done by using the Archimedes method, image analysis was used for porosity measurement of only those coupons which had high levels of porosity. Three cross section images were captured using an optical microscope (Olympus MX51) at 50X magnification level from locations in the center areas of XY and YZ planes of selected coupons. These images were then converted into de-noised black-and-white micrographs using the porosity analysis program developed in MATLAB. Circularity, which serves as the morphology descriptor of pores, was also calculated using this program.

Microstructural characterization techniques

The specimens were prepared using standard metallographic specimen preparation methods. 10% oxalic acid was used in the electrolytic etching process [4]. Microstructures in both XY and YZ planes of 12 as-built coupons were observed using an optical microscope and SEM.

Average diameter of columnar austenitic grains for each specimen were calculated based on randomly chosen SEM images at high magnification levels where γ grains grows perpendicular to the XY plane (ASTM E112-12). At least two SEM images for the purposes of calculation of average grain diameter were captured for each specimen.

Phase proportion analysis based on X-ray diffraction

X-ray diffraction (XRD) analysis (Bruker D8 diffractometer system) was carried out at room temperature. Thin specimens for XRD analysis were cut parallel to the XY plane using a low speed diamond saw. 2θ values were set bounded in between 30° and 90° for all the specimens. After obtaining XRD graphs, the volume fraction of martensitic phase V_M for each specimen was calculated using equation (4) below, where n_M and n_A are the numbers of the (hkl) line for which the integrated intensities have been measured for α' and γ phases, I_M^{hkl} and I_A^{hkl} are α' and γ peak intensity values for corresponding (hkl) planes, and R_M^{hkl} and R_A^{hkl} are α' and γ theoretical relative intensity factors for corresponding (hkl) planes. The corresponding theoretical relative intensity factors for Cu Kα radiation XRD were calculated by Jatczak et al.[8].

$$V_M = \frac{\frac{1}{n_M}\sum_0^n\left(I_M^{hkl}/R_M^{hkl}\right)}{\frac{1}{n_A}\sum_0^n\left(I_A^{hkl}/R_A^{hkl}\right) + \frac{1}{n_M}\sum_0^n\left(I_M^{hkl}/R_M^{hkl}\right) + V_C} \tag{4}$$

<u>**Results and discussions**</u>

The results below show the influences of energy density on porosity, microstructures and martensitic phase proportion of 17-4PH stainless steel coupons under various SLM processing parameters.

Porosity analysis of as-built test coupons

(a) Porosity based on Archimedes method

Based on the Archimedes method, figures 3 and 4 show the density values of coupons fabricated using the two sets of processing parameters shown in table 2. The standard deviations indicated as the error bars (same for all following figures) for density measurement are less than 0.004g/cm^3 for all coupons.
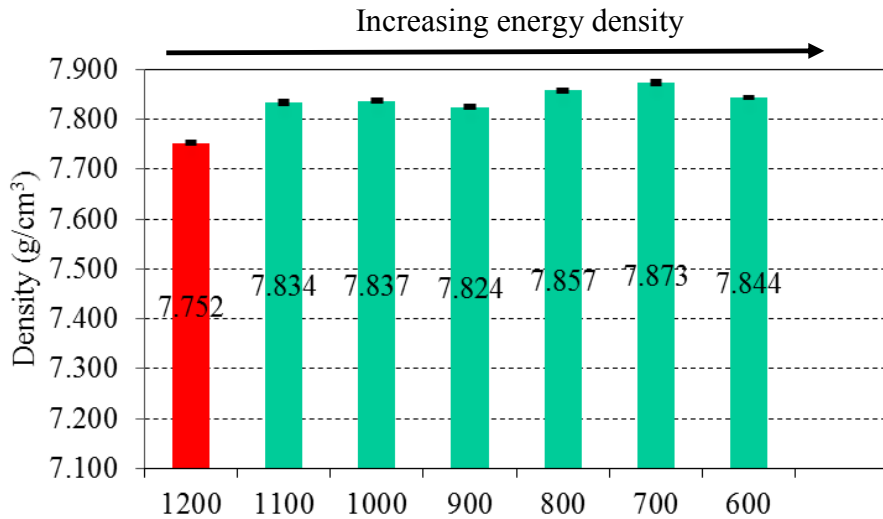
Figure 3 Density values of coupons manufactured under various energy densities (195W laser power)

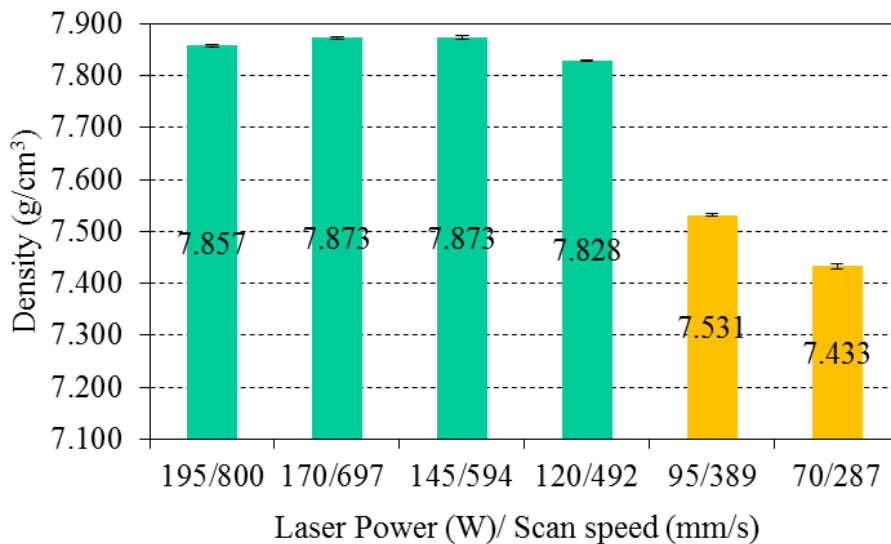*Error bars represent standard deviations.

Figure 4 Density values of coupons manufactured using a constant energy density of 61J/mm^3

According to figures 3 and 4, the overall density level for as-built coupons is above 7.8 g/cm^3. A noticeable drop in coupon density is observed at 41J/mm^3 (195W/1200mm/s), a very low energy density level. However, even at a so-called "optimal energy density level," a dramatic density decrease occurs when both laser power and scan speed are below 95W and 389 mm/s respectively.

Approximately 100% fully dense part can be built using EOS recommended processing parameters [6]. Therefore 7.857 g/mm^3, which is the density value achieved using 195W laser power and 800mm/s scan speed, is selected as the full density threshold value ρ_{tv} in this study. Figure 5

displays the porosity values corresponding to density values using the conversion equation (3). For parameter sets consisting of varying energy densities, parts are almost fully dense with a maximum of 0.4% porosity when energy density varies from 44-81 J/mm^3. However, when energy density drops to 41 J/mm^3 (195W/1200/mm/s), a noticeable 1.3% porosity could be observed. Meanwhile, for parameter set consisting of a constant energy density level, coupons with both low laser power and scan speed illustrate significantly higher porosities. The result suggests that energy density may not be a good indicator for porosity level of SLM manufactured coupons when processing at low speeds and laser powers.
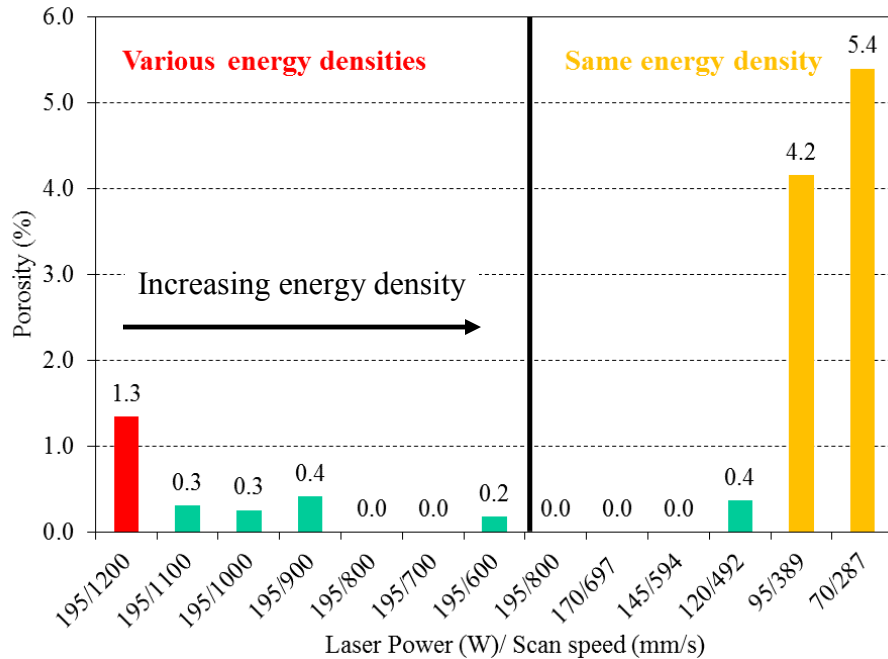
Figure 5 Porosity for coupons manufactured using different processing parameters

Left: Porosity at various energy densities   Right: Porosity at the same energy density 61 J/mm^3

(b) Analysis of porosity formation mechanisms

Figures 6, 7, and 8 show SEM images for pore morphology using processing parameters of 195W/1200mm/s, 95W/389mm/s and 70W/287mm/s respectively, where porosities are significantly higher than for other parameters.
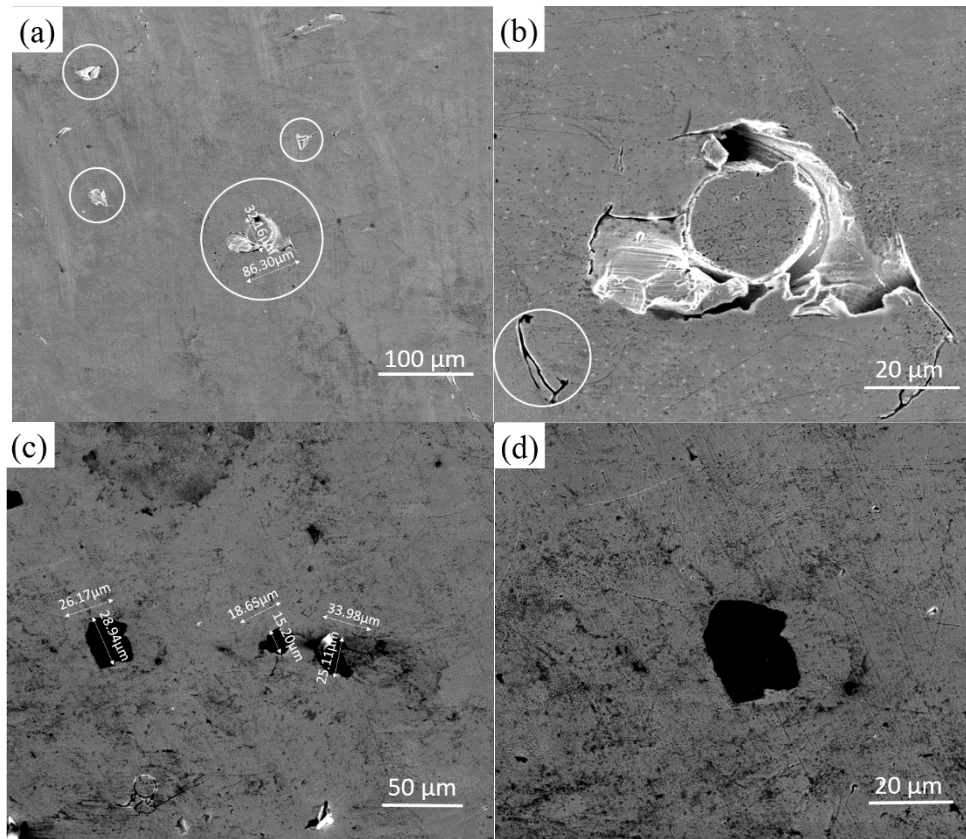
479

Figure 6 SEM image for pore morphology using 195W laser power and 1200mm/s scan speed

Upper row: XY plane   Lower row: YZ plane

For low energy density with both high laser power and scan speed (195W/1200mm/s), pore sizes are significantly smaller, and very few un-melted particles are observed in figures 6 (a) and (c). These are very different from the pores which occur in coupons manufactured using optimal energy density with both low laser power and scan speed (95W/389mm/s and 70W/287mm/s), where large caves and crevices are formed in figures 7 (a)&(c), and 8 (a)&(c) with many un-melted particles. This is likely due to differences in porosity formation mechanisms. For processing parameters of 195W/1200mm/s, the laser input is sufficient to completely melt stainless steel powders due to a high laser power level. When a very high scan speed is applied, however, the laser scan track may show discontinuity due to the balling phenomenon as shown in figure 6 (b). Such balling effects are possibly the consequence of an unstable melt pool; very high scan speeds will apply much more shear stress to the liquid phase which generates higher surface tension inside the melt pool, leading to a high likelihood of ball formation. The splashes of liquid balls caused by very high scan speeds will also contribute to porosity under such processing conditions [2,9]. It is also worth noting that more thermal-induced cracks can be found in such processing conditions, since extremely high cooling rates caused by very high scan speeds lead to higher thermal stress, resulting in -z-propagating cracks as shown in figure 6 (b).
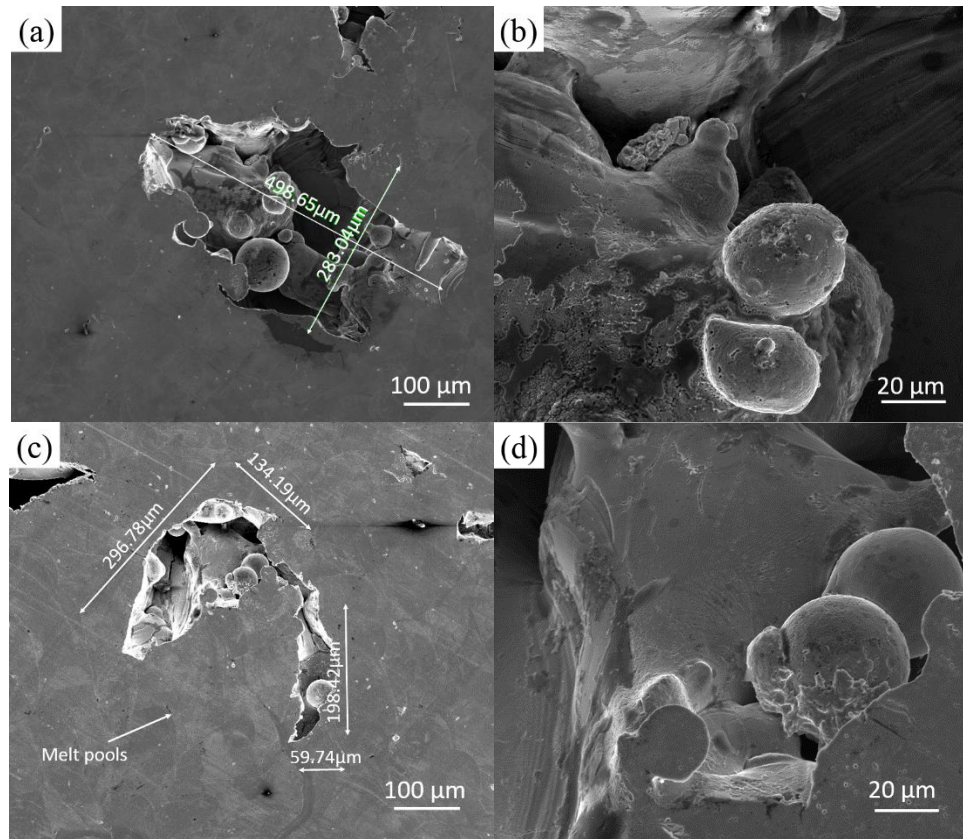
Figure 7 SEM image for pore morphology using 95W laser power and 389mm/s scan speed

Upper row: XY plane   Lower row: YZ plane

For processing parameters of 95W/389mm/s and 70W/287mm/s, the laser input is low due to a lower laser power level even though the corresponding energy density levels are at an optimal value. This resulted in insufficient melting where only a limited liquid phase was formed. The viscosity of the melt pool increases when a combination of un-melted balls and a liquid phase is present, which has a negative influence on the flowability of the liquid [2]. Meanwhile, the laser beam under low laser power level may not be able to penetrate all the way to the previous solidified layer for newly formed liquid to attach, resulting in poor wetting. A lower laser power may also mean that there is less likelihood of powder ablation and plasma formation near the surface of the powder bed, thus lessening the overall "absorptivity" of the powder at lower laser powers. The consequence of these various potential mechanisms is that large caves and crevices were formed with many un-melted and half-melted particles inside.
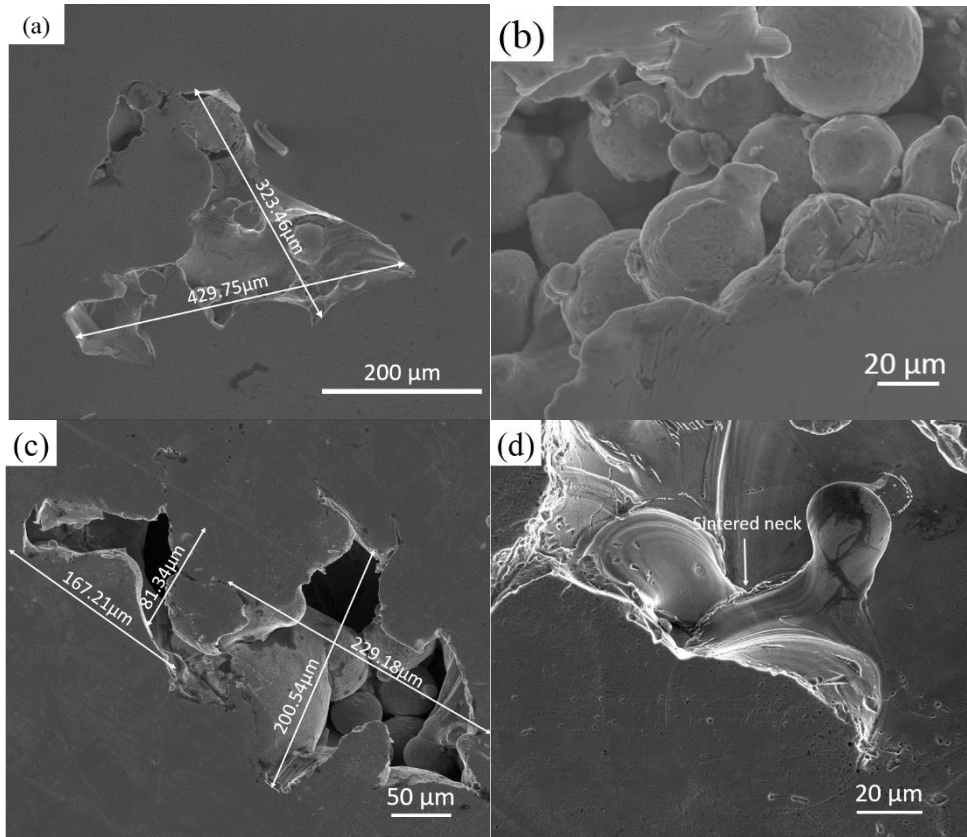
Figure 8 SEM image for pore morphology using 70W laser power and 287mm/s scan speed

Upper row: XY plane   Lower row: YZ plane

(c) Porosity and pore morphology characterization based on image analysis

For coupons with the highest porosity values, image analysis was used to compare and quantitatively characterize pore morphology by introducing circularity as a descriptor. Circularity is described as equation (5), where SF is shape factor ranging between 0 and 1, A is the pore area and P is the pore perimeter. The closer SF is to 1, the more circular is a given pore [10,11].

$$\text{SF} = \frac{4\pi A}{P^2} \tag{5}$$

Figure 9 shows the comparison of porosity values acquired using the Archimedes method and image analysis. For lower porosity, image analysis may not be able to appropriately represent the porosity due to large variations compared to Archimedes method. However, with the increase of porosity level, image analysis shows almost the same porosity level as Archimedes method does.
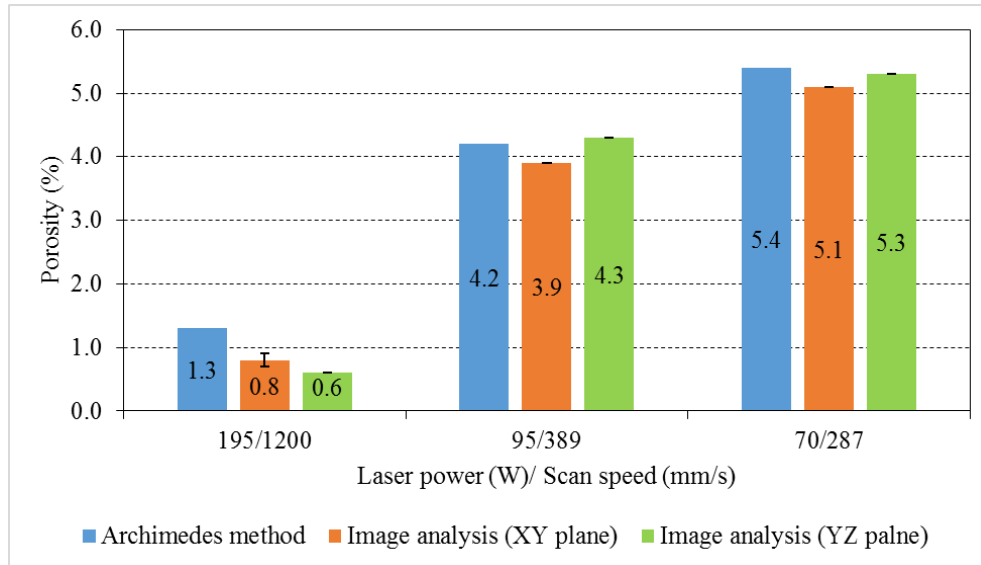
Figure 9 Comparison of porosity values between the Archimedes method and image analysis

The comparison of pore circularity values of the 3 most porous coupons is shown in figure 10. Large standard deviations in circularity within 3 SEM images in the XY plane for each coupon indicate that there is a large variation in the circularities of the pores for coupons manufactured using the same processing parameters. Coupons which were fabricated using both low laser power and scan speed show an overall more irregular morphology. This may be due to the large crevices caused by un-melted powders under insufficient laser input, compared to the pores formed during very high laser power and scan speed where small pores are formed mainly due to the gaps between balls as discussed in the last section. Therefore for smaller pores, such as the ones formed using 195W/1200mm/s parameters, they exhibit more regular shapes.
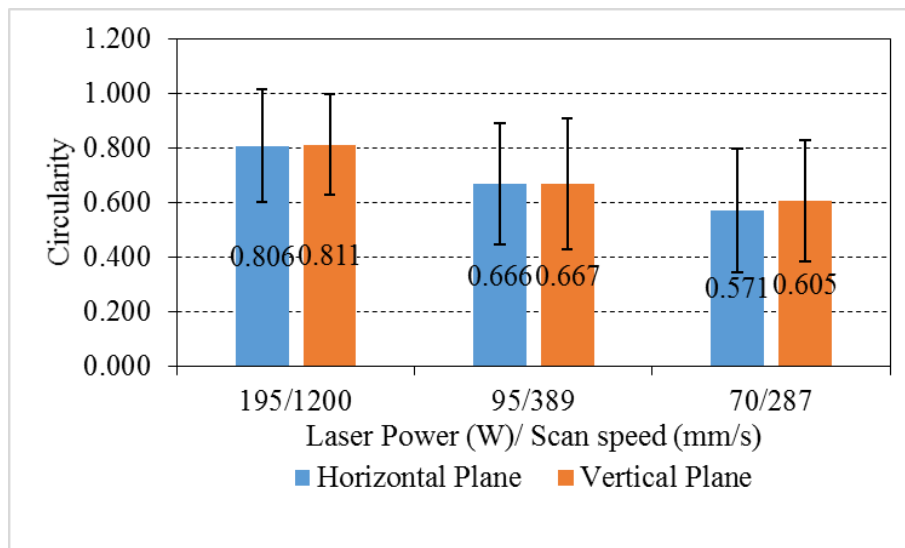

Figure 10 Pores circularity of porous coupons based on image analysis

Microstructural analysis of specimens

SEM was used for microstructural observation of as-built coupons at different magnification levels after electrolytic etching. Figure 11 shows an array of micrographs in XY and YZ planes of coupons fabricated using various laser power and scan speed levels (parameters are shown as the white labels on the top right corner of each image).
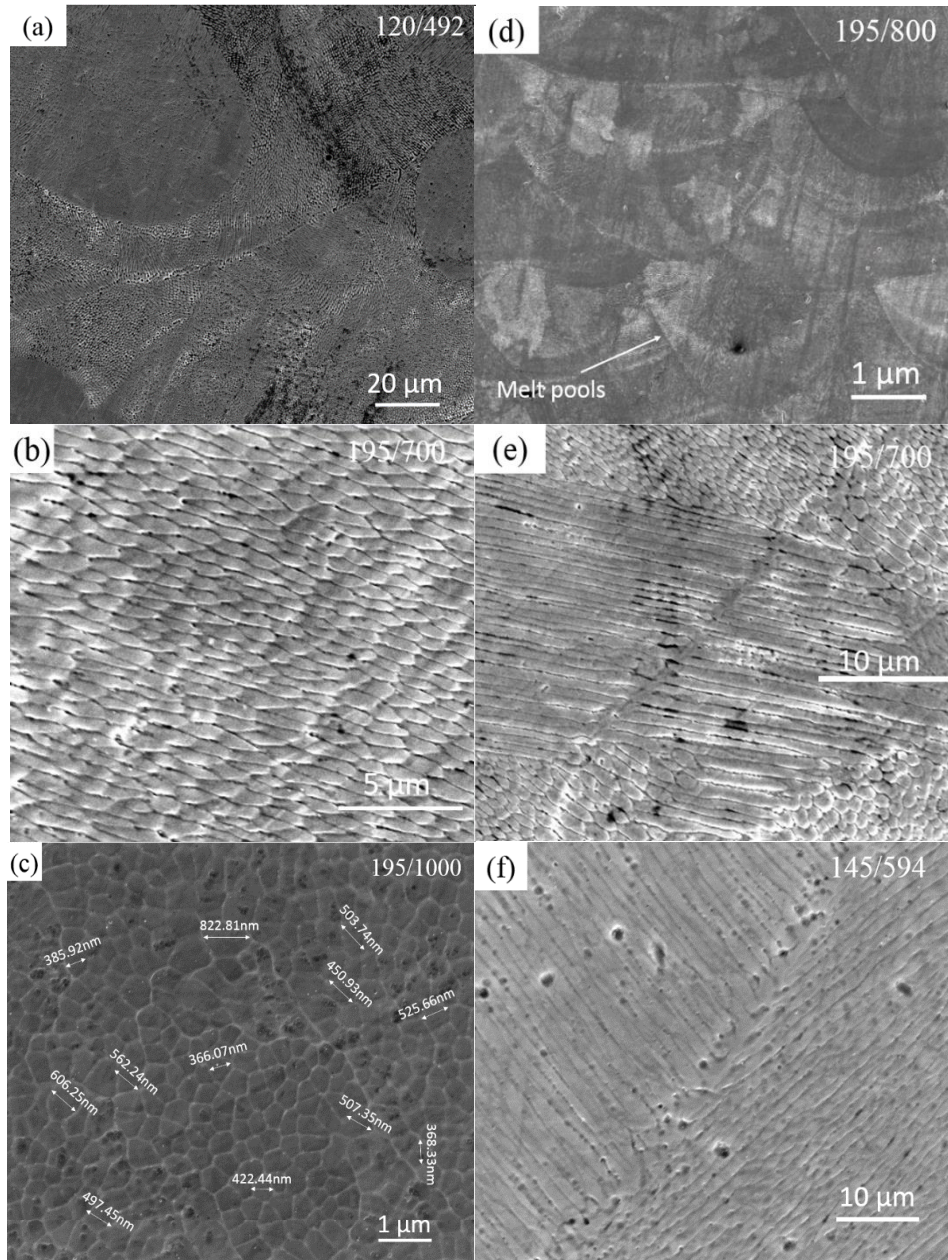

Figure 11 Typical SEM micrographs in XY and YZ planes using various processing parameters in SLM

Left column: XY plane   Right column: YZ plane

Figure 11 (d) shows the typical macrostructure of 17-4PH stainless steel fabricated using SLM at lower magnification. The overlapping, bowl-shaped features on the YZ plane are formed in the melt pool solidification process. These melt pool features, which are created by each laser scan, are parallel to the build direction. Parallel columnar austenitic grains can be observed at higher magnification levels due to their very fine sizes, shown in figure 11 (b), (c), (e) and (f). The columnar grains show strongly preferred orientation since they grow along with the heat transfer directions in both XY and YZ planes.

Figure 11 (c) is one of the SEM images used for calculation of average diameter of the columnar austenitic grains, where the γ grain grows perpendicular to the XY plane. Austenitic grain diameters under both processing parameter sets were calculated and the results are shown in figures 12 and 13.
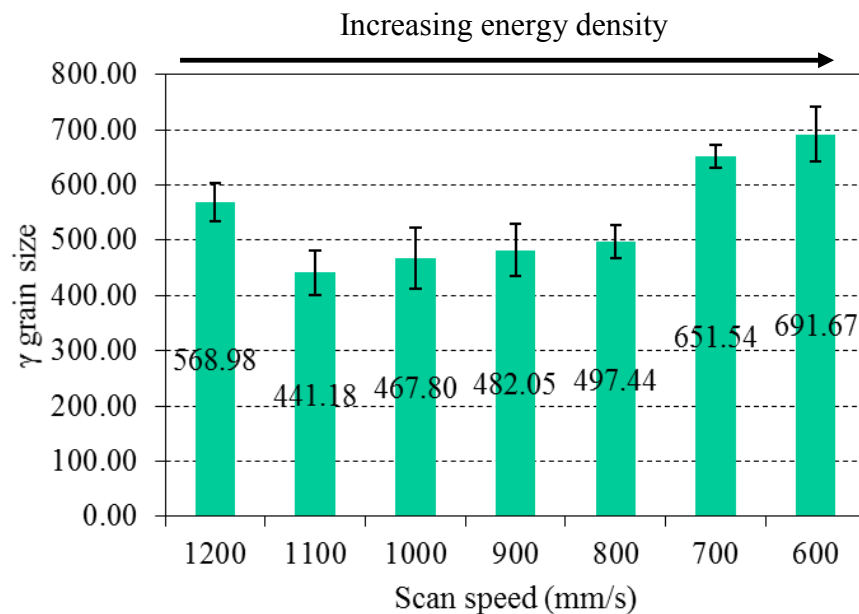

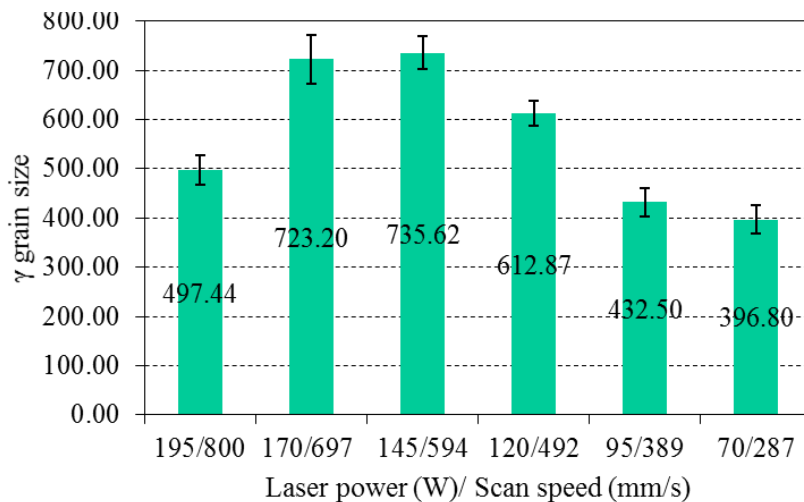Figure 12 Austenitic grain diameters under various energy densities (195W laser power)

Figure 13 Austenitic grain diameters under constant energy density 61 J/mm3

In figure 12, the grain diameter increases with decreasing laser scan speed, except for at the highest scan speed of 1200mm/s. This overall trend is due to the fact that at scan speeds there is a lower cooling rate and higher average melt pool temperature, giving the austenitic grains more time to grow. However, a competing mechanism must have become relevant at the maximum scan rate. It could be that the increase of γ grain diameter which occurred in the highest scan speed (1200mm/s) condition was due to the decreased thermal conductivity which results from porosity and cracks in the microstructure. This decreased thermal conductivity could result in lower overall cooling rates at this parameter set and thus larger grains.

Using constant energy density but different laser power and scan speed combinations, the γ grain diameter exhibits a maximum at mid-range combinations of parameters and decreases in diameter at high and low scan speeds (see figure 13). One possible explanation is that when the laser power is at a higher value ranging from 195W to 145W, the corresponding laser input is sufficient to create a stable melt pool at a high temperature. Grain size will be scan speed dependent in this region, which gives a trend similar to figure 12. However, as the laser power drops to a low level below 145W, even though the energy density is constant, the absorbed energy in the material become insufficient, resulting an unstable melt pool with lower overall temperature. In consequence, γ grain diameter will be laser power dependent; the lower the laser power, the less time for grains to grow due to the lower temperature of the melt pool.

Analysis of martensitic phase proportion in specimens

An XRD graph, is shown in figure 14, represents the phase information of coupons manufactured using 70W laser power and 287mm/s scan speed. Due to the strongly preferred orientation of γ columnar grains in the material, peak intensities of different crystal planes for each phase have been considered. (110), (200) and (211) planes are selected to represent the α' phase, and (111), (200), (220) planes are selected to represent the γ phase.
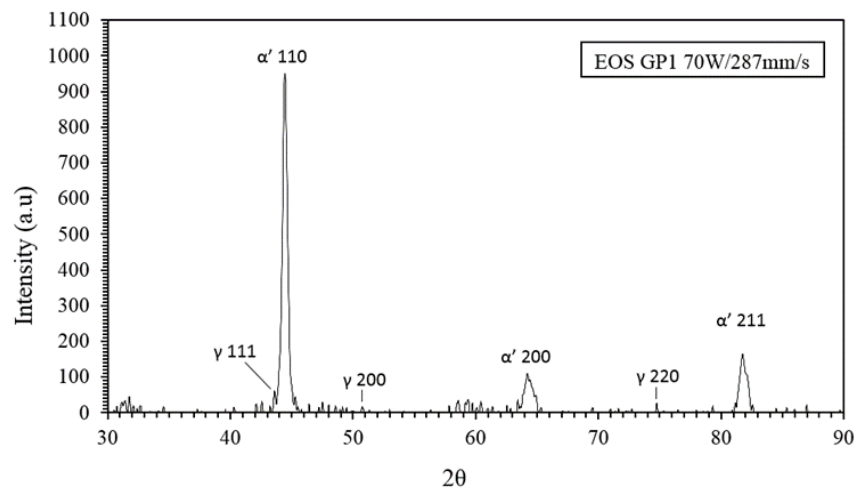

Figure 14 XRD graph for coupon manufactured at 70W laser power and 287mm/s scan speed (XY plane)

After the calculation using equation (4), the volume fraction values of martensitic phase V_M for each specimen are shown in figure 15. It appears that the volume fraction of α' phase stays at a similar level, approximately 70% in coupons manufactured under all processing conditions. The results may be due to the very fast cooling rates occurring in all SLM processes using parameters discussed in this study. All cooling rates are much faster than the critical cooling rate V_c in the CCT diagram for 17-4PH stainless steels. Therefore, all coupons may achieve similar proportions of α' and γ phases during martensitic transformation. In addition, 70% martensitic level for the material tested in this experiment is lower than that for LPW-procured 17-4 stainless steel powders the where α' phase is at least 82% under the same processing parameters [4]. The GP1 powder used in this experiment is atomized in a nitrogen atmosphere and nitrogen is known to be an "austenite stabilizer", while LPW 17-4 powder is atomized within argon, thus explaining the difference in martensitic transformation.
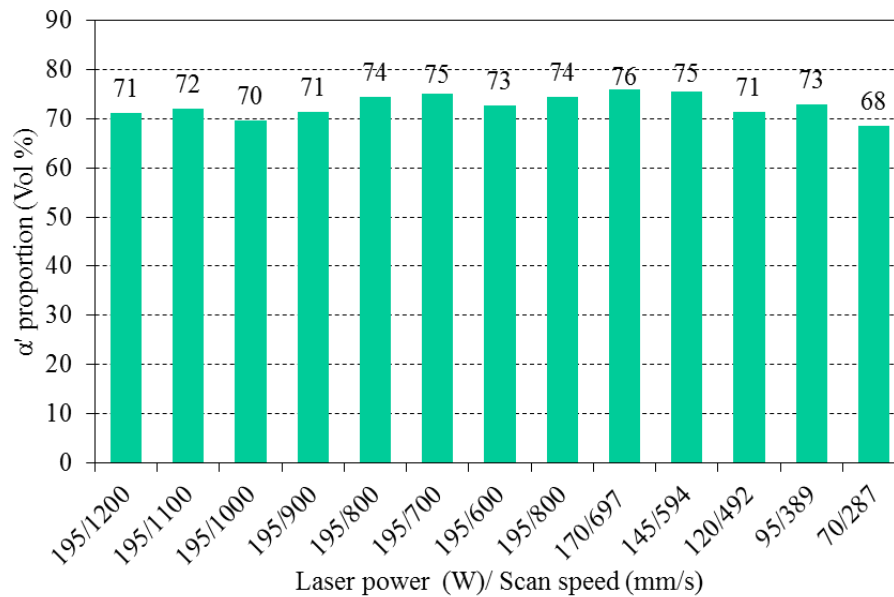
Figure 15 Volume fraction of martensitic phase in coupons manufactured under all processing parameters

Conclusions

12 test coupons using 17-4PH stainless steel powders have been successfully manufactured using an EOS M270 DMLS machine. Two sets of processing parameters were applied; one where various energy density levels were obtained by changing the scan speed while keeping laser power constant, and the other set consisting of a constant energy density where changes in laser power were matched by scan speed changes to keep overall energy density the same.

Various experiments and analysis have been done to the as-built test coupons in order to determine the influence of energy density, a key factor in the selective laser melting process, on porosities and microstructures of as-built parts.

Energy density may not be a good indicator for porosity level of SLM manufactured parts. Coupons fabricated using the same "optimal" energy density level using different laser powers and scan speeds show significantly different levels of porosity from each other, up to a maximum value of 5.4%.

Two types of porosity formation mechanisms were identified and discussed. Balling phenomena and high thermal stress cracking are mainly responsible for the porosity which occurs at very high laser power and scan speed, while insufficient melting is the primary reason for crevices filled with many un-melted powders at very low laser power and scan speed. Also, pores in coupons manufactured using both high laser power and scan speed exhibit smaller size and more circular shape in comparison with coupons manufactured using both low laser power and scan speed.

Some typical SLM meso-structural features such as overlapping, bowl-like melt pools, and microstructural features such as very fine, parallel columnar austenitic grains were observed using SEM. Columnar austenite grains show strongly preferred orientation in SLM. With a decrease in scan speed at a constant high laser power, there exists an increasing trend for average diameters of austenitic grains. However, when laser power drops to a certain level, austenitic grain size may become primarily dependent on laser power.

Volume fraction values of martensitic in GP1 stainless steel coupons are all at approximately 70%, which indicates differences in processing parameters used in this study may not have a significant influence on phase proportions in as-built parts.

Future works

Although this work provides insight into microstructural features of parts made using these parameters, no experiments were performed to determine the effect on mechanical properties of these parameters. Mechanical tests are required to find a correlation between mechanical properties and the processing parameters.

Acknowledgements

References

[1] Thijs L., Verhaeghe F., Craeghs T., Humbeeck J.V., Kruth J.P. (2010). "A study of the microstructural evolution during selective laser melting of Ti–6Al–4V." *Acta Meterialia* 58: 3303-3312.

[2] Li, R., Liu, J., Shi, Y., Wang, L., & Jiang, W. (2012). Balling behavior of stainless steel and nickel powder during selective laser melting process. *The International Journal of Advanced Manufacturing Technology*, *59*(9-12), 1025-1035.

[3] Facchini, L., Vicente, N., Lonardelli, I., Magalini, E., Robotti, P., & Molinari, A. (2010). Metastable Austenite in 17–4 Precipitation-Hardening Stainless Steel Produced by Selective Laser Melting. Advanced Engineering Materials, 12(3), 184-188.

[4] Starr T.L., Rafi K., Stucker B., Scherzer C.M. (2012). "Controlling phase composition in selective laser melted stainless steels." *Proceedings of 2012 Solid Freeform Fabrication Symposium*, the University of Texas, Austin.

[5] Facchini, L., Vicente, N., Lonardelli, I., Magalini, E., Robotti, P., & Molinari, A. (2010). "Metastable Austenite in 17–4 Precipitation-Hardening Stainless Steel Produced by Selective Laser Melting." *Advanced Engineering Materials*, *12*(3), 184-188.

[6] Material data sheet for EOS Stainless Steel GP1 for EOSINT M270.

[7] Spierings, A. B., Schneider, M., & Eggenberger, R. (2011). Comparison of density measurement techniques for additive manufactured metallic parts.*Rapid Prototyping Journal*, *17*(5), 380-386.

[8] Jatczak, C. F. (1980). Retained Austenite and its Measurement by X-ray Diffraction. *Society of Automotive Engineers,*, 20.

[9] Gu, D., & Shen, Y. (2009). Balling phenomena in direct laser sintering of stainless steel powder: metallurgical mechanisms and control methods.*Materials & Design*, *30*(8), 2903-2910.

[10] Mikli, V., Kaerdi, H., Kulu, P., & Besterci, M. (2001). Characterization of powder particle morphology. *Proceedings of the Estonian Academy of Sciences: Engineering (Estonia)*, *7*(1), 22-34.

[11] Hentschel, M. L., & Page, N. W. (2003). Selection of descriptors for particle shape characterization. *Particle & Particle Systems Characterization*, *20*(1), 25-38.